



Numerical and experimental investigation of the in-phase and out-phase plasma actuation effects on the wake flow for $Re = 1000$

N. Nabatian*

Faculty of Mechanical and Energy Engineering, Shahid Beheshti University, Tehran, P.O. Box 16589-53571, Iran.

Received 26 June 2021; received in revised form 2 April 2022; accepted 28 November 2022

KEYWORDS

Dielectric barrier discharge plasma actuator;
 Symmetric pattern;
 Active control;
 POD;
 DMD.

Abstract. The current study aims to characterize the role of symmetric pattern in the flow control induced by dielectric barrier discharge plasma actuators. To this end, two Dielectric Barrier Discharge (DBD) actuators were used for in-phase excitation with a duty cycle of 50%, thus leading to symmetric wake pattern and out-phase excitation at two pulsing frequencies of $St = 0.2$ and $St = 1$ at $Re = 1000$ which form quasi-symmetric and asymmetric flow structures, respectively. The modes obtained from Proper Orthogonal Decomposition (POD) and Dynamic Mode Decomposition (DMD) methods highlight the competition between the symmetric (S) and asymmetric (K) modes in all cases. The harmonic in-phase plasma actuation with a duty cycle of 50% is the most effective flow control method with the lowest power consumption. The harmonic out-phase excitation is not much effective; however, adjustment of the actuator position can form a symmetric pattern with minimum power consumption. Although superharmonic out-phase plasma actuation reduces the wake region, it does not significantly affect the lift reduction and consumes a high amount of energy, indicating that the phase difference and plasma location affect the size and symmetry of the vortical structure. Based on the symmetry properties of the designed wake pattern formed by frequency and phase difference of the plasma actuator, an effective active flow control can be ensured. The numerical results were validated based on the conducted experiments.

© 2023 Sharif University of Technology. All rights reserved.

1. Introduction

The flow around a cylinder has different flow regimes based on its Reynolds number. At $Re = 48$, the flow breaks its time continuous invariance and exhibits a periodic behavior known as von Karman vortex street. At $Re > 200$, the purely periodic behavior loses its stability, and its nonlinear evolution appears.

Flow properties are altered by Reynolds number as the bifurcation parameter, leading to the structure vibration. Extensive studies have been conducted on Vortex Induced Vibration (VIV) observed in various applications such as pipelines on the seabed and in the tubular-and-shell heat exchangers, offshore structures, wind turbine blades, and compressor cascade. The control of the unsteady flow detached from the body in the form of wake region can reduce the forces exerted on the structure and prevent the failure of structures.

A variety of methods have been developed for flow control and they are categorized into passive and active forms. Plasma actuation as one of the efficient

*. Tel.: +98 21 73932733

E-mail address: n.nabatian@sbu.ac.ir (N. Nabatian)

active flow control methods is commonly applied in different kinds of bodies such as bluff body, airfoils, and flat plate [1–5]. Plasma actuators were used for flame stabilization application. The annular Dielectric Barrier Discharge (DBD) actuator was mounted on the bluff body surface and operated by square wave, and higher variation rate of voltage induced the secondary low pressure region in addition to the co-flow recirculation zone formed by bluff body itself, which in turn enhanced the flame stabilization [6].

The DBD was employed to control the flow separation over an airfoil at different angles of attack in a range higher than stall, leading to the higher lift-to-drag ratio than that of a well-designed airfoil. The continuous DBD plasma actuator at the unity burst frequency improved the lift coefficient of the turbulent separated flow over NACA0015 at Reynolds number 1.6×10^6 . A pairing of large vortices was induced in the vicinity of the airfoil surface to energize the boundary layer and delay the separation. The high-frequency actuation from the leading edge decreased the drag coefficient with laminar separation bubble length reduction [7]. The DBD plasma actuators were used for pitch stability control of NACA0012 airfoil at a small Reynolds number. The co-flow plasma outperformed the counter flow configuration in controlling the pitch instability at the laminar separation fluttering [8]. The DBD with Direct Current Augmented (DCA) actuator was employed to control the flow over an NACA0012 airfoil with $Re = 2.01 \times 10^5 - 3.35 \times 10^5$. The active electrode and DCA were mounted at 18% and 48% chord of airfoil at low angles of attack, respectively. The results demonstrated that upon increasing the DCA through the sawtooth-shape electrode, the lift and drag would increase and decrease, respectively [9]. The plasma actuation was used for dynamic stall control of large wind turbine blades. Upon inducing vortices in the vicinity of the suction surface, a virtual bulge was formed which added momentum to the boundary layer and expanded the low-pressure region. As a result, the stall angle was delayed, hence drag reduction, lift enhancement, and hysteresis loop region reduction [10]. The unsteady pulse plasma controlled the dynamic stall by inducing a negative pressure region on the suction side of the airfoil. The obtained results highlighted the duty cycle and pulsed frequency as the main parameters involved in the unsteady dynamic stall flow control [11].

The flow control was experimentally conducted around a cylinder by two plasma actuators at $Re = 10000$. The vortices induced by plasma, transferred momentum to the cylinder surface, which is similar to Moving Surface Boundary Layer Control (MSBLC) mechanism using the counter-rotating control cylinder for drag reduction. This mechanism was called virtual MSBLC. Two different functioning mechanisms of the

surface DBD actuators were studied in [12,13]. At low Reynolds numbers, DBD produces mean force and ionized wind. At higher velocities, in the case of applying high-voltage Nanosecond Dielectric Barrier Discharge (NS-DBD), gas heating at the DBD wall generates pressure pulses, modifying the near wall flow. The optimum performance of the DBD was experimentally assessed by altering the shape of the powered electrode and its dimensions to intensify the thrust force imposed on the flow [14,15]. The mechanisms of streetwise vortex generation were studied by analyzing the effect of some parameters such as flow velocity, length of actuator, used materials, and forcing amplitude on the streetwise vortex in a boundary layer of a flat plate [16]. The effect of the Three-Electrode Discharge (TED) actuators on the cylinder wake was investigated for $Re = 5500$ and a drag reduction of 40% was achieved. Due to the limitation of the maximum induced velocity magnitude at higher Re values, the efficiency was reduced and different arrangements of actuators in the streamwise and spanwise directions should be used to prevent the flow separation [17,18]. To overcome this problem, a new stair-shaped dielectric barrier was designed with the aim of induced flow velocity enhancement and mechanical efficiency improvement without affecting the DBD durability. In this new design, the thickness of the dielectric barrier decreased along the covered electrode which, in turn, caused a higher plasma discharge and, consequently, higher induced velocity [19]. To optimize the flow control configuration, the passive and active control mechanisms were simultaneously used including wavy leading-edge airfoils with curved multi-electric DBD plasma actuators. This hybrid system made flow transition faster and this phenomenon caused earlier flow reattachment with less noise [20]. The spatial-temporal vortex structure induced by an AC DBD plasma in quiescent air with PIV was experimentally investigated. According to the results, vortex shedding frequency was scaled with force coefficient. With force coefficient enhancement, the speed of vortex roll up increased, which led to the formation of lower space between vortices and reduction of the dominant frequencies downstream [21]. However, vortical structures in the flowing fluid differed from the quiescent air with variations in the voltage input time and burst ratio. In the quiescent air, the vortex was in circular form, and the positive vortex collided with the forward negative vortex, merged, and shed downstream, while in the flowing fluid, the vortex was stretched and vortices did not merge due to the acceleration of the flow when leaving the surface [22]. As different physical mechanism underlies the flow control at various regimes, a fundamental study of the plasma effect on the flow structure is of importance. When these plasma discharges are applied to manipulate the flow

perturbations, the spatial and temporal evolution of the flow field characteristics should be deeply investigated to understand the plasma actuator control mechanism. The objective of the present study was to investigate the symmetry role of the dominant wake pattern, influenced by different excitation frequencies and phase difference of the plasma actuators on the flow control.

2. Theoretical background

In previous studies [23–25], through Proper Orthogonal Decomposition (POD) analysis, 2D wake was shown to have two fastest growing modes containing almost 90% of the total fluctuating energy in different flow regimes. These modes were, therefore, used to model the flow dynamics. The low-order one-dimensional oscillatory pattern can be expressed as follows:

$$v(x, y, t) = S(t)e^{i\left(\frac{x}{\lambda_S} + \omega_S t\right)} f(y) + K(t)e^{i\left(\frac{x}{\lambda_K} + \omega_K t\right)} g(y) + c.c., \quad (1)$$

where $f(y)$ and $g(y)$ are the corresponding symmetric and asymmetric eigenfunctions, respectively, which represent the velocity profiles, while $S(t)$ and $K(t)$ are the time-dependent amplitudes. These two dominant modes are characterized by specific symmetry properties. The ‘symmetric’ mode (S) has reflection symmetry with respect to the y -axis and translational symmetry, as well.

$$v(x, y, t) = v(x, -y, t) = v(x + \lambda_S, y, t) = v(x, y, t + \tau_S), \quad (2)$$

while mode K is invariant with respect to the evolution of half of its shedding period and reflection in y :

$$v(x, y, t) = v(x, -y, t + \tau_K/2) = v(x + \lambda_K/2, -y, t), \quad (3)$$

where $\tau_S = 2\pi/\omega_S$, and $\tau_K = 2\pi/\omega_K$. This two-mode approximation of the fluctuating velocity field satisfies the linearized Navier-Stokes equations and can be used for stability analysis. Since these two primary modes have well-defined symmetries, the complex amplitude equations governing the nonlinear interaction of $S(t)$ and $K(t)$ can be derived through equivariant bifurcation theory based on the requirement that the velocity field should remain unchanged under the action of the symmetries. The overall spatio-temporal symmetry group is $SO(2) \times Z_2(\kappa) \times S^1 = O(2) \times S^1$ where κ acts through reflection represented as $Z_2(\kappa)$, T acts through translation given by $SO(2)$, and S^1 represents the θ phase shift symmetry.

$$\kappa : y \rightarrow -y \Rightarrow \kappa(S, K) = (S, -K)$$

$$T : x \rightarrow x + l\lambda_S \Rightarrow T(S, K) = (Se^{inl}, Ke^{iml})$$

$$\theta : t \rightarrow t + \theta\lambda_S/2\pi \Rightarrow \theta(S, K) = (Se^{in\theta}, Ke^{im\theta}). \quad (4)$$

The general form of the evolution amplitude equations based on the set of invariants and equivariant functions is presented below. The detailed derivation of the equations can be found in [24].

$$\begin{aligned} \frac{dS}{dt} = & [(\xi_0 + i\gamma_0) + (\xi_1 + i\gamma_1)|K|^2 + (\xi_2 + i\gamma_2)|S|^2 \\ & + (\xi_3 + i\gamma_3)(K^n \bar{S}^m)^2]S + [(\eta_0 + i\kappa_0) \\ & + (\eta_1 + i\kappa_1)|K|^2 + (\eta_2 + i\kappa_2)|S|^2 \\ & + (\eta_3 + i\kappa_3)(K^n \bar{S}^m)^2]K^{2n} \bar{S}^{2m-1}, \end{aligned} \quad (5a)$$

$$\begin{aligned} \frac{dK}{dt} = & [(\alpha_0 + i\delta_0) + (\alpha_1 + i\delta_1)|K|^2 + (\alpha_2 + i\delta_2)|S|^2 \\ & + (\alpha_3 + i\delta_3)(K^n \bar{S}^m)^2]K + [(\beta_0 + i\mu_0) \\ & + (\beta_1 + i\mu_1)|K|^2 + (\beta_2 + i\mu_2)|S|^2 \\ & + (\beta_3 + i\mu_3)(K^n \bar{S}^m)^2]\bar{K}^{2n-1} S^{2m}. \end{aligned} \quad (5b)$$

The low-order model with complex coefficients, when solved numerically with variation of the bifurcation parameters, captures the frequency variation of the main modes as well as nonlinear interaction between modes with coupling terms. In the present study, bifurcation coefficients for linearized Navier-Stokes equations are a function of the phase difference and frequency of the controlled pulse induced by the plasma actuation. The steady lower-order symmetry subgroups, which bifurcate from the symmetry group, are determined through equivariant bifurcation theory, considering variations in the bifurcation parameters. Given that the asymmetric Karman shedding as the first mode should be controlled, the second symmetric mode should be energized to interact with (and thus control) the mode K . Three cases are considered to study the resulting forced wake dynamics. The harmonic symmetric excitation with frequency $f_e = f_s$, asymmetric harmonic excitation with half a cycle phase difference between the plasma actuators, and superharmonic asymmetric actuation with the forcing frequency of $f_e = 5f_s$ to observe the asymmetric actuation effect on the wake pattern.

2.1. Data reduction

2.1.1. Proper orthogonal decomposition

As shown in Eq. (6), the mean velocity field is subtracted to obtain the fluctuating velocity components. The perturbed flow field is a function of time and space $V' = v'(x, t)$, where x represents the spatial coordinates and t refers to the time. The eigenfunctions

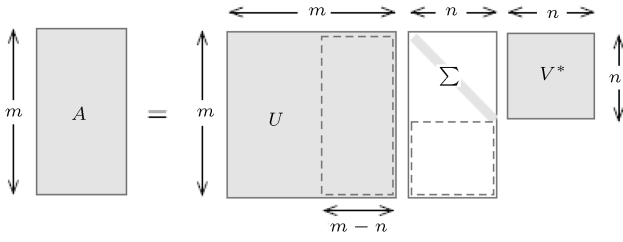


Figure 1. Singular Value Decomposition (SVD) of a matrix A [19].

of the velocity field data matrix are determined via POD.

$$A = v'(x, t) = v(x, t) - \bar{V}(x). \quad (6)$$

Since the flow data is a rectangular matrix, two sets of the eigenvectors given in Figure 1 are decomposed.

$$AV = U\Sigma, \quad (7)$$

where $V = [v_1 \ v_2 \ \dots \ v_n]$ and $U = [u_1 \ u_2 \ \dots \ u_m]$ are the right and left singular vectors, respectively, while Σ is the diagonal matrix including the eigenvalues $\sigma_1 \geq \sigma_2 \geq \dots \geq 0$. Then, the singular value decomposition of the velocity field is in the form of $A = U\Sigma V^T$.

The covariance matrix based on the higher resolution of the spatial or temporal discretization is defined as $C = AA^T$. The eigenvalue problem is solved through $CW = \Lambda W$ to determine the eigenvectors $W(t)$ and eigenvalues matrix Λ including $\lambda_i = \varphi_i^2$. The dominant normalized spatial modes $U = [\varphi_1 \ \varphi_2 \ \dots \ \varphi_i]$ are calculated through Eq. (8):

$$\varphi^i(x) = \frac{\sum_{n=1}^k W^i(t^n) v'(x, t^n)}{\left| \left| \sum_{n=1}^k W^i(t^n) v'(x, t^n) \right| \right|}. \quad (8)$$

The right singular vectors including POD coefficients $\theta = \sum_{i=1}^N a_i$ are obtained by back-projecting the velocity field to the left singular vectors:

$$\theta = U^T V'. \quad (9)$$

As shown in Eq. (10), the low-order velocity field is reconstructed from the N dominant orthogonal modes, thus minimizing the magnitude of $\sum_{i=1}^N |v'(x, t) - \sum_{i=1}^N a_i(t) \varphi_i(x)|^2$ based on the least square method:

$$v'(x, t) = \sum_{i=1}^N a_i(t) \varphi_i(x), \quad (10)$$

where φ_i is the normalized spatial basis function called Topos, and a_i is the related time-dependent coefficient quantifying the fluctuating kinetic energy of each mode known as Chronos.

2.1.2. Dynamic mode decomposition

The temporal evolution of the sequential velocity field

snapshots is modeled based on the Dynamic Mode Decomposition (DMD) method. Then, in addition to the frequency variation, the amplitude changes can be captured for dominant modes. A set of snapshot pairs separated with a constant time step after temporal mean subtraction is arranged, as shown in Eq. (11):

$$X_1 = [x(t_1) \ x(t_2) \ \dots \ x(t_m)] \in R^{n \times m}, \quad (11a)$$

$$X_2 = [x(t_2) \ x(t_3) \ \dots \ x(t_{m+1})] \in R^{n \times m}. \quad (11b)$$

These consecutive snapshots are linearly related with a propagator operator known as Koopman operator. The propagator B is calculated by multiplying both sides by X^T and inverting the spatial covariance matrix $X_1 X_1^T$; then, we have:

$$X_2 = B X_1, \quad (12a)$$

$$\begin{aligned} X_2 &= B X_1 \rightarrow X_2 X_1^T = B X_1 X_1^T \\ &\Rightarrow B \approx X_2 X_1^T (X_1 X_1^T)^{-1}. \end{aligned} \quad (12b)$$

Due to the presence of noise in the experiments, a more robust DMD algorithm is achieved by filtering the low-energy flow dynamics by applying the POD to the sequential snapshots before DMD to ensure the decomposition convergence. The data set X is decomposed through SVD method to $X = U\Sigma V^T$, where U contains the spatial modes, V refers to the temporal content, and Σ includes the fluctuating energy of the corresponding POD modes. The first r POD modes, $X_1 = U_r \Sigma V_{r,1}^T$ and $X_2 = U_r \Sigma V_{r,2}^T$, eliminate the noise effect and they are assumed to have the same spatial structures and differ only in the shift of temporal structures. Then, substituting the reduced SVD basis and multiplying Eq. (12b) with transpose of the spatial modes reduced the propagator, as shown in Eq. (13), based on the assumption that $U_r^T U_r = I$ where I is the identity matrix. Since the least square calculation of the propagator B is computationally expensive, its companion approximation S is computed from Eq. (13), and the linear dynamic system is fitted to the reduced space model.

$$\begin{aligned} X_2 &= B X_1 \rightarrow U^T [U \Sigma V_2^T = B U \Sigma V_1^T] \\ &\rightarrow \underbrace{\Sigma V_2^T}_{Y_2} \approx \underbrace{U^T B U}_S \underbrace{\Sigma V_1^T}_{Y_1}, \\ S &\approx U_r^T (U_r \Sigma V_{r,2}^T V_{r,1} \Sigma^{-1} U_r) U_r \\ &= \Sigma V_{r,2}^T V_{r,1} \Sigma^{-1}. \end{aligned} \quad (13)$$

The eigenvectors and eigenvalues of matrix B are approximated by eigendecomposition of matrix S from $S v_i = \mu_i v_i$, where μ_i is the complex eigenvalue for the corresponding eigenvector v_i . Every DMD mode is constructed via multiplying U including global

spatial modes to the eigenvector extracted from matrix S given in Eq. (14a), while the corresponding complex eigenvalue of each DMD mode is calculated from Eq. (14b). The modulus of the complex DMD eigenvalues is approximately equal to 1.

$$\varphi_i = Uv_i, \tag{14a}$$

$$\lambda_i = \frac{\ln(\mu_i)}{\Delta t}. \tag{14b}$$

The real component of $\sigma_i + i\omega_i = \lambda_i$ determines the growth/decay rates, while the imaginary part corresponds to a single characteristic frequency of the spatial mode. This computationally less expensive propagator is used in Dantec’s software Dynamic Studio [26,27].

$$x(t) = \Sigma \varphi_i e^{\lambda_i t} = \Sigma_i \varphi_i e^{\sigma_i t} e^{i\omega_i t}. \tag{15}$$

3. Experimental setup

As shown in Figure 2, the plasma actuator includes two electrodes separated by a dielectric material flush-mounted symmetrically on each side of the cylinder wall close to the separation point of the flow since more effective wake structure modification can be ensured

with lower energy. One of the electrodes is exposed to the air, while the other one is covered by dielectric material. The electrodes are made of copper foil tape with the thickness and width of 0.05 mm and 10 mm, respectively, for the encapsulated electrode, while the exposed one is 4 mm wide. Five layers of 0.1 mm Kapton tapes are used as a dielectric to prevent the inner discharge. A pair of exposed electrodes is supplied with 10 kV high AC voltage with 2.5 kHz carrying frequency, while the encapsulated electrodes are grounded. Due to the high amplitude of the electric field, the neutral gas is ionized. The ionized gas creates an electric force that causes the momentum exchange between the charged and neutral particles in the direction of discharge. This ionic wind modifies the flow properties close to the wall and since its velocity is low, the streamwise velocity data is the extracted 3D downstream.

The electric circuit consists of a signal generator, amplifier, and ignition coil. The high frequency signal is generated in LabView software where carrying frequency, signal shape, modulation frequency, and duty cycle can be set, as demonstrated in Figure 3. At the high carrying frequency of $f = 2.5$ kHz, the negative sawtooth shape is formed due to its long discharge time,

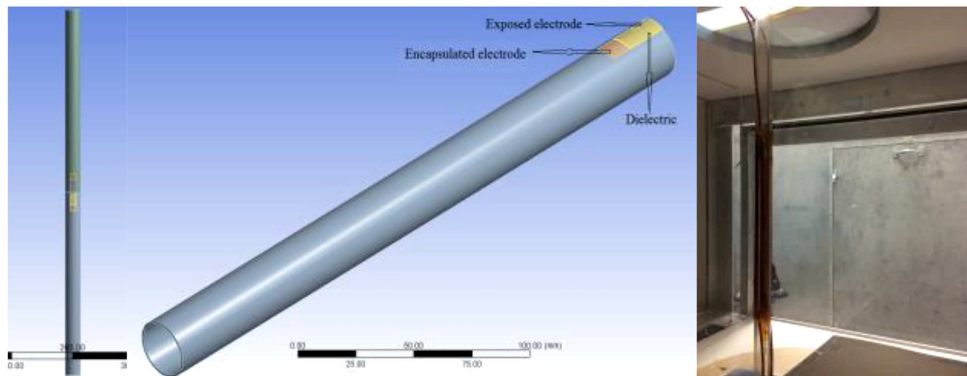


Figure 2. Schematic and experimental set up of plasma actuators installed on the cylinder.

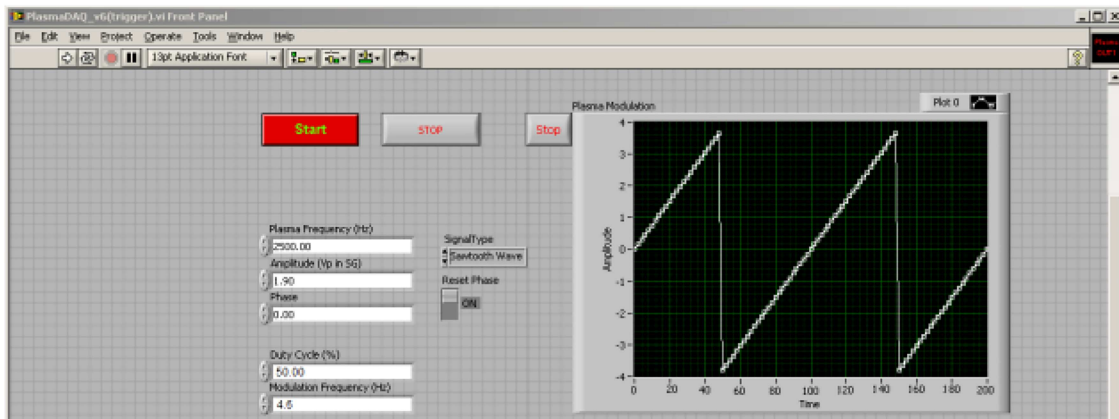


Figure 3. LabView interface for signal generation of harmonic in-phase plasma actuators.

leading to higher body force. In the negative sawtooth, the signal shape requires less dV/dt to ignite the plasma as the electrons leave the surface of the electrode, while in the positive signal, more dV/dt is required since the electrons should deposit the dielectric surface which is more resistant than the former. Two time periods are defined here: the time interval T_e is related to the excitation frequency which equals the vortex shedding frequency $T_e = 1/f_e$ for the harmonic case. The actuator is only active in the percentage of the modulation time interval T_2 , which is defined as a duty cycle parameter T_2/T_e . Upon using an NI analogue output card, the input signal is coupled to an audio amplifier feeding an ignition coil, which produces a high voltage signal at 10 kV. The output voltage and current are measured using probes.

Figure 4 shows the experimental setup including a cylinder with the diameter of $D = 25$ mm located in a closed-loop wind-tunnel with a test section of 610 mm \times 610 mm at $Re = 1000$. Since the ratio of the wind tunnel width to the cylinder diameter is 24, the blockage effect is ignored. The velocity field measurement is performed by 2D PIV, which includes

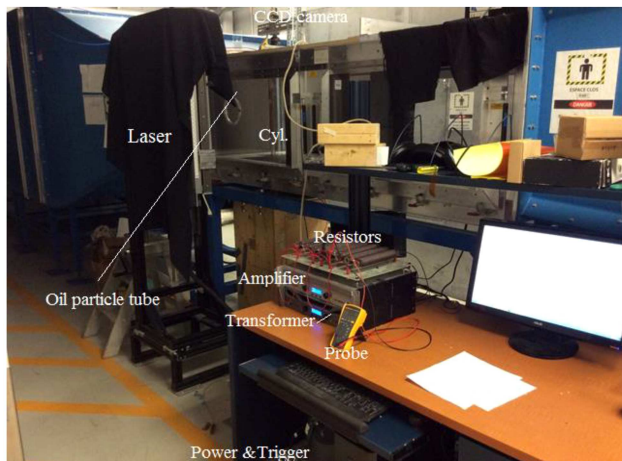


Figure 4. Experimental set up of plasma actuation used for flow control.

an atomizer, laser, CCD camera, and a synchronizer. The $11 \mu\text{m}$ olive oil particles formed by a PIVTEC GmbH seeding generator are uniformly distributed in the flow field. A two-rod Nd:YAG pulsed laser illuminates the horizontal plane of flow field at the mid-span of the cylinder with a stable laser sheet. It was synchronized with the camera connected to a PC using Dantec's Dynamic Studio software.

To reduce the reflection effect, the lateral walls are covered with black papers. A Flow Sense 2M/E CCD camera equipped with 62 mm Nikon F-mount lens with the capability of recording double frame pairs of images is mounted normal to the laser sheet. The time lapse between two frames set is $50 \mu\text{s}$, and the imaging region resolution is 1600×1200 pixels. The images are recorded by CCD camera for 12s including 55 cycles of the harmonic plasma actuation with 15 Hz sampling frequency. An average of 180 images was used to produce the mean velocity field, which resolves the temporal dynamic behavior of flow field within one unsteady actuation period. The Dantec Dynamic Studio software controls the laser and camera and conducts the post processing of the acquired images transferred through NI acquisition cards to it.

4. Numerical set up

The pulsed plasma actuation is simulated in ANSYS-CFX with incorporation of a source term into the momentum equation. Then, mesh convergence test was performed in [23-25]. $y^+ = 0.06$ was set to correctly model the boundary layer with 109692 elements, as shown in Figure 5. Shear Stress Transport (SST) model was used for turbulence modeling. The pressure-velocity coupling at a time step of $1/100f_e$ was modeled through SIMPLE method. The velocity inlet boundary condition of 0.6 m/s corresponding to $Re = 1000$, the pressure outlet with 0Pa , and no-slip condition for cylinder wall were set. The lateral boundaries are free stream walls, while the sidewalls are considered

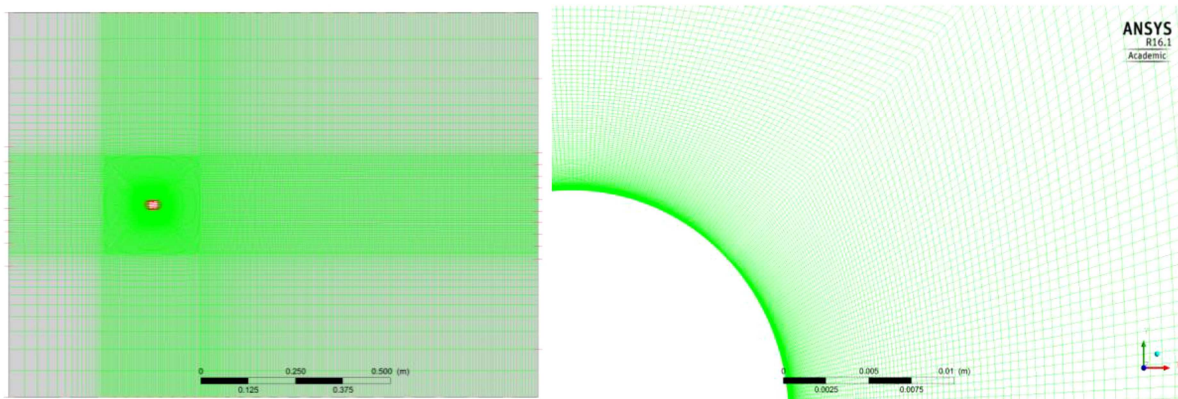


Figure 5. Two-dimensional domain with structured mesh.

zero shear symmetry boundary condition. The plasma actuation acts as a wall jet transferring a momentum to the flow with a body force. This is modeled in CFX by adding a source term into the momentum equation with an expression given in Eq. (17c) [28]. The area of the region where the plasma was applied is calculated by multiplication of the length of the encapsulated electrode with its thickness as $4 \text{ mm} \times 6 \text{ mm} \times 1000 \text{ mm} = 24000 \text{ mm}^3$. The source strength is proportional to the plasma power. This power is introduced as a force density term through dividing it by the cell weight in units of N/m^3 , as presented in Eq. (17b). The input power is calculated from the enhancement of the kinetic energy, as shown in Eq. (16b):

$$\Delta KE = Power \times \Delta t, \tag{16a}$$

$$KE_1 = KE_0 + \Delta KE \Rightarrow \frac{1}{2} m u_1^2 = \frac{1}{2} m u_0^2 + \Delta KE \Rightarrow u_1 |u_1| = (u_0 |u_0|) + \frac{2\Delta KE}{m}, \tag{16b}$$

$$u_1 = \sqrt{(u_0 |u_0|) + \frac{2(Power \times \Delta t)}{\rho V_{cell}}}, \tag{16c}$$

$$a = \frac{u_1 - u_0}{\Delta t}, \tag{17a}$$

$$f_v = \frac{F}{V} = \frac{m \cdot a}{V} = \rho \cdot \frac{u_1 - u_0}{\Delta t}, \tag{17b}$$

$$f_v = \rho \frac{\sqrt{(u_0 |u_0|) + \frac{2(Power \times \Delta t)}{\rho V_{cell}}} - u_0}{\Delta t}, \tag{17c}$$

where ρ is the fixed fluid density, m the cell mass, and u_0 the initial velocity. Although the energy component is enhanced due to the plasma actuation, its magnitude is not constant and is triangular in shape; however, the body force is assumed fixed in this simulation for the sake of simplicity. The total plasma force depends on the mesh size that is calculated through an expression, which integrates the strength in the plasma located cells to ensure the exertion of the specific body force. The unsteady actuation period was obtained from the natural shedding frequency given by the Strouhal number. The time step is defined as $T/100$, which is equal to $0.00217s$. The duty cycle period is set at 50%.

5. Results and discussion

To study the effect of plasma actuation on the cylinder wake flow, first, a natural vortex shedding was simulated. Figure 6(a) shows the periodic oscillation of the lift force for the unactuated flow. In the spectral analysis of the lift force perturbation in Figure 6(b), the non-dimensional shedding frequency was obtained as 0.2. The snapshots of the velocity field over a shedding cycle are given in Figure 7 where a vortex sheds in half a cycle from each side of the cylinder.

The 3D downstream velocity fluctuations were extracted and stored in a matrix to analyze the wake

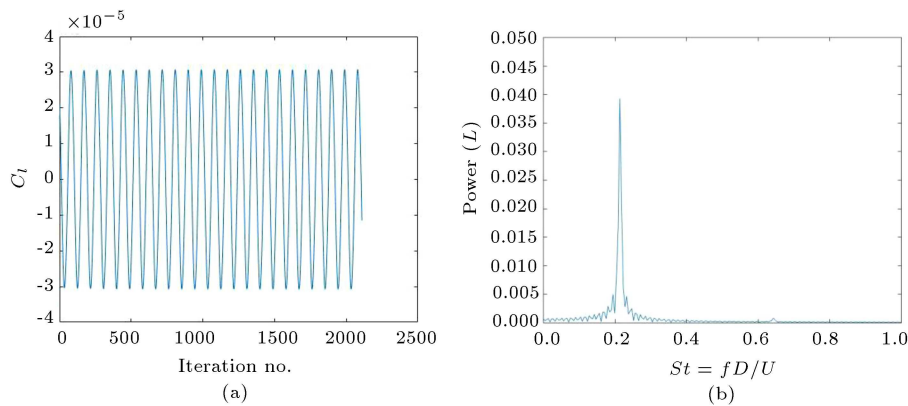


Figure 6. The lift force with its spectra for no control flow.

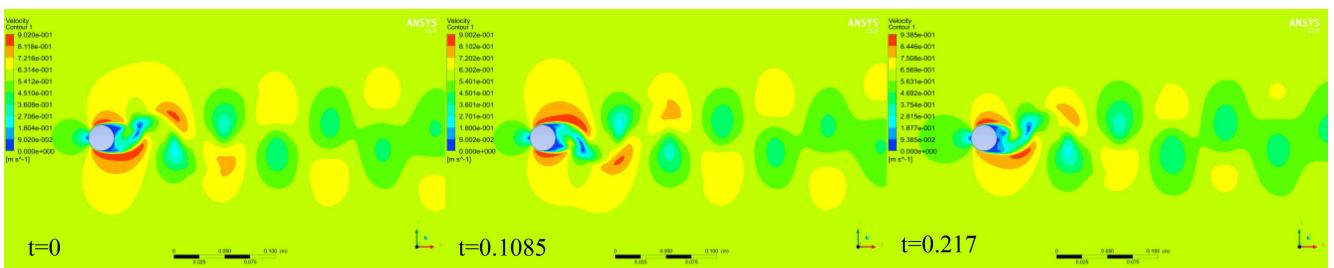


Figure 7. The snapshots of velocity field for no control flow over shedding cycle.

dynamics by POD. The POD analysis of velocity field for unactuated flow confirmed that the two modes contained almost 90% of the total fluctuating kinetic energy and could globally represent the flow field, as shown in Figure 8. The patterns of the higher modes are almost similar to those of the lower ones; however, as the mode number increases, smaller vortex structures are observed due to the lower energy. The first spatial mode (Topos) with its related temporal mode (Chronos) is shown in Figure 9(a) and (b), indicating the asymmetric Karman shedding (K), while the second Topos with its related time evolution (Chronos)

is the symmetric mode (S). Time evolution of the dominant flow pattern reconstructed by the first two POD modes is depicted in Figure 10.

The flow stability analysis was conducted on the time-resolved data based on the DMD algorithm at a sampling frequency of 15 Hz. The complex eigenvalue of the first mode is $0.9959 + 0.073i$. The real part characterizes the decay rate and the imaginary part corresponding to angular velocity $33.7s^{-1}$ representing the dynamical behavior of a natural vortex shedding. The first mode oscillates with a single non-dimensional frequency $St = 0.22$ and the second mode with $St = 0.47$ that is superimposed on the primary one

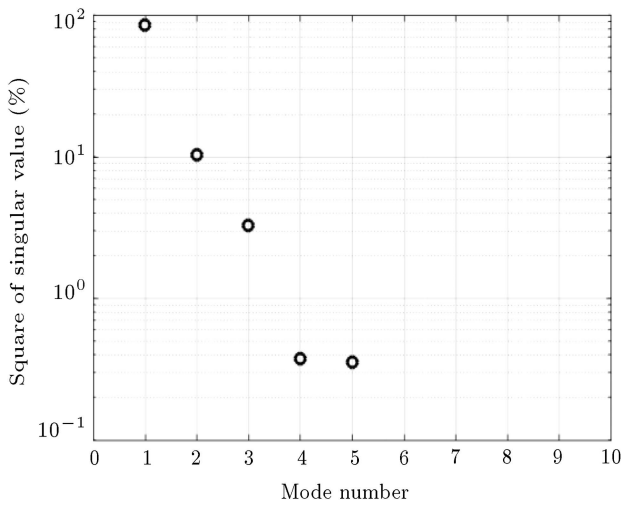


Figure 8. Eigenvalues of the velocity perturbation for no control flow.

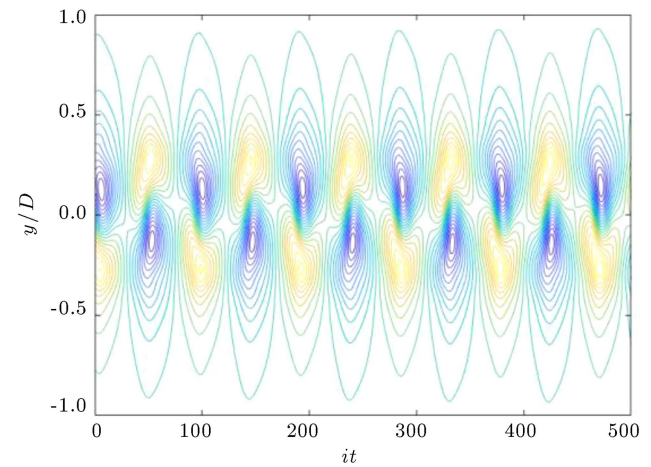


Figure 10. Reconstructed temporal evolution of velocity field using 2 primary POD modes for no control case.

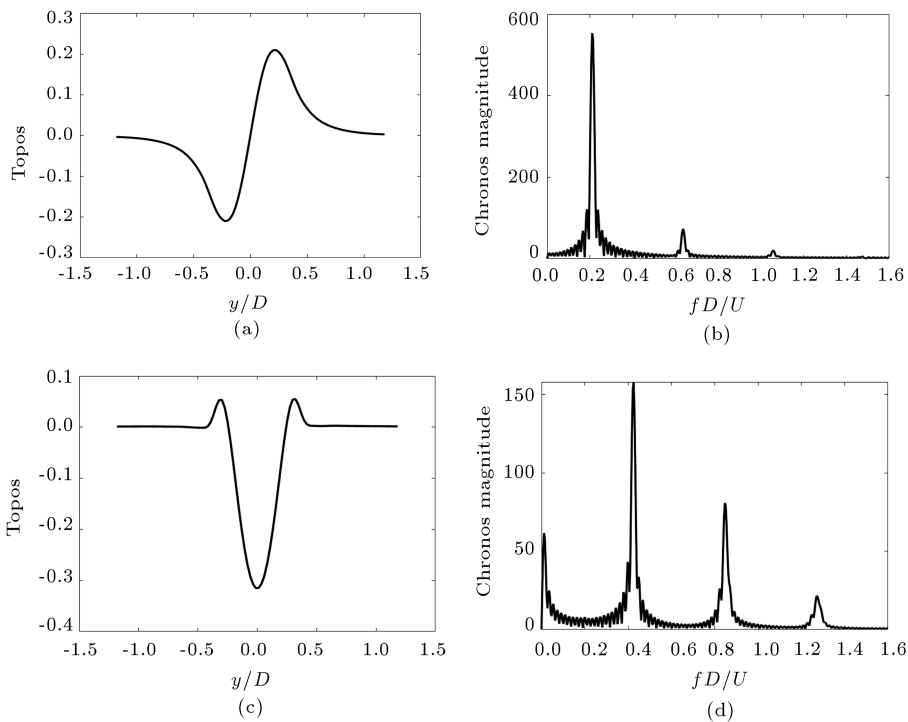


Figure 9. Topos and Chronos of two dominant POD modes of no control flow.

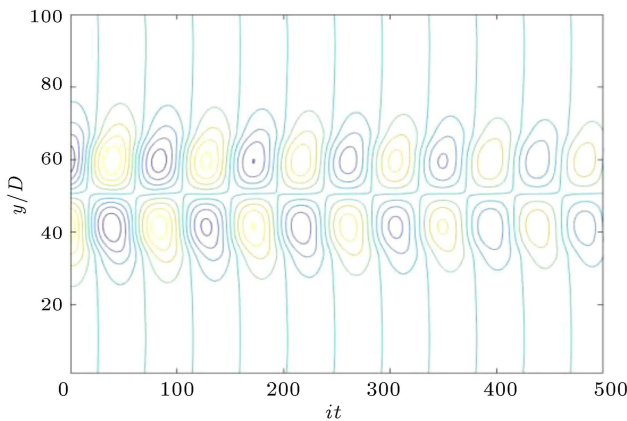


Figure 11. Reconstructed temporal evolution of velocity field using 2 primary DMD modes for no control case.

where a high decay rate of the second mode makes the first mode structure the dominant wake structure. A comparison of Figures 10 and 11 shows that the reconstructed wake structure from two stable modes illustrates the dynamics of the flow spatial structures associated with Karman shedding. However, the POD is also applied to the complex data to represent the temporal evolution of the flow field; however, due to the difference in algorithms, POD analysis cannot capture the growth/decay rate of mode amplitude.

In-phase pulsed actuation: By activating harmonic in-phase excitation, the lift becomes 10 times smaller than the natural shedding lift force given in Figure 12(a). The oscillating amplitude decreased while the periodic behavior still exists, indicating the vortex shedding phenomenon. Due to the nonlinearity of the flow dynamics influenced by harmonic in-phase plasma actuation, there are several frequencies in the lift force; however, the main peak is located at a non-dimensional frequency of $St = 0.2$.

The sequences of instantaneous snapshots of velocity contours are given in Figure 13 to represent the flow field modification over an excitation cycle for pulsed harmonic in-phase plasma actuation. Two

symmetric vortices are initiated since the in-phase plasma is activated. Between the times $t = 0.0542s$ and $t = 0.108s$, the induced vortices grow and start to shed simultaneously. Since the duty cycle is at 50%, the momentum source is turned off at the halfway point of the shedding cycle when the velocity decreases dramatically up to the end of the cycle, as observed in the lift force behavior through a comparison of Figure 12(a) and Figure 13. In the beginning of the next cycle, the plasma actuators are again activated during the forcing time. The in-phase plasma actuation adds momentum to the boundary layer by exciting the resonance of the turbulent flow structure at the shedding frequency to mix lower momentum flow in the boundary layer with the higher momentum outer flow. The pulsed in-phase actuation creates the symmetric velocity field with lower aerodynamic force amplitude, which is used for flow control.

To ascertain that the dominant modes can represent the impact of plasma actuation, the velocity field modal decomposition by POD is conducted. The percentage of contribution of POD modes in the total fluctuating kinetic energy of the flow field for harmonic in-phase excitation is given in Figure 14. It indicates that the first two modes contain most of the energy, while the energy of the first asymmetric mode K for the unactuated flow diminishes considerably. Instead, the symmetric spatial mode S energy is enhanced through in-phase actuation and consequently, the first pair of modes is symmetric, while the second pair associated to the asymmetric mode K shifts to the 3rd and 4th modes. The Chronos related to the first two symmetric modes given in Figure 15 have peaks at $St = 0.2$ corresponding to the natural shedding frequency. The reconstructed wake flow pattern with two POD modes is shown in Figure 16, where the symmetric velocity pattern dominates the asymmetric vortex shedding, confirmed by the velocity contours given in Figure 13.

DMD of the harmonic in-phase plasma actuation has an imaginary part of the first and second modes related to $St = 0.28$ and $St = 0.88$, respectively. The

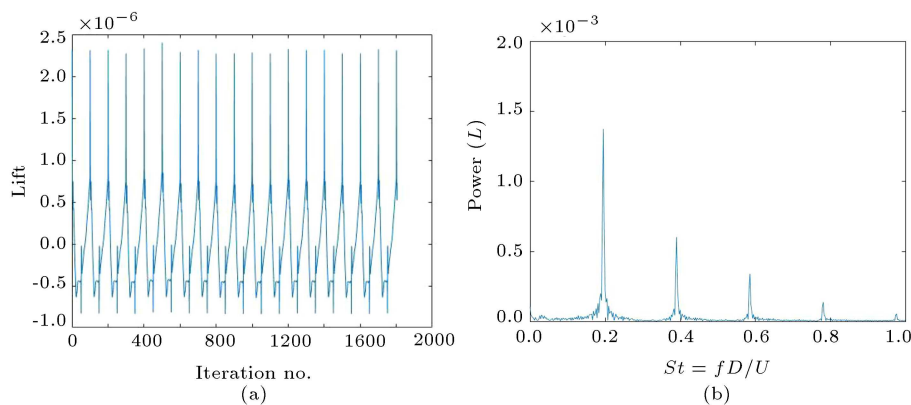


Figure 12. Lift and its spectra for harmonic in-phase plasma actuation with 50% duty cycle.

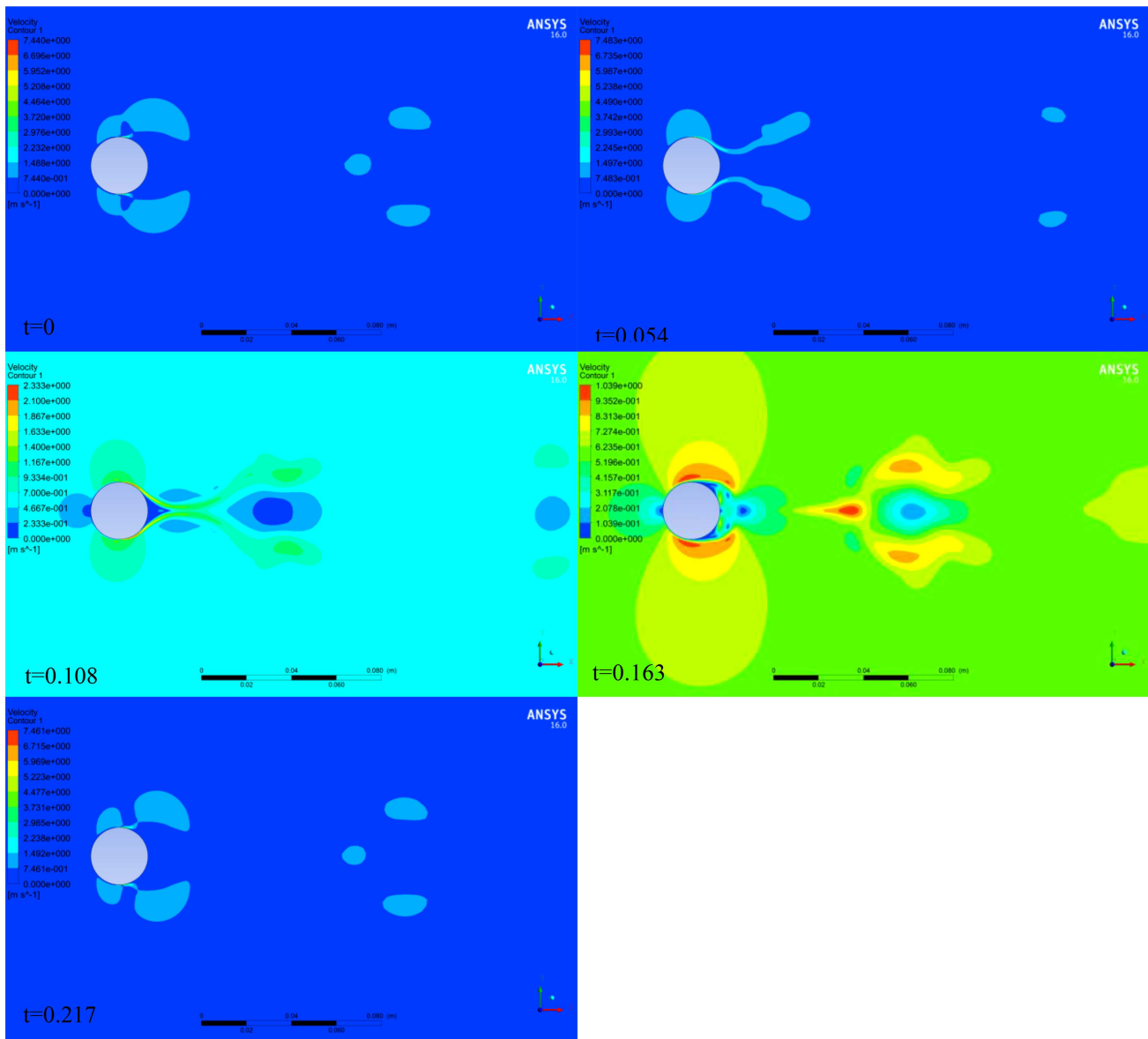


Figure 13. The snapshots of velocity field over an excitation cycle for pulse harmonic in-phase plasma actuation with 50% duty cycle.

quasi-periodic symmetric flow structure dynamics is observed in Figure 17 from the superposition of two stable modes. The second mode frequency in the DMD analysis is different from that in the POD since the POD spatial modes are ranked based on their energy level while the DMD ensures a more stable frequency of the related spatial structure.

Out-of-phase pulsed actuation: Two types of out-of-phase actuation were studied in this paper: harmonic excitation with natural shedding frequency and superharmonic with a frequency of $f_e = 5f_s$. In the harmonic plasma activation, while the lower-side shear layer flow starts to separate and a larger vortex is formed, the momentum source with a fixed strength equal to the in-phase excitation is activated from the

upper side of the cylinder, leading to a trapped vortex. However, the size of the induced vortex is smaller than that of the natural vortex. The plasma switching logic opposite to the naturally shedding vortex is controlled using the lift coefficient. After half of the excitation cycle, the plasma is switched to the lower side where a formed vortex from the upper side sheds and the smaller vortex continues to grow, and vice versa, in the next half of the cycle.

The lift does not change significantly as shown in Figure 18(a). The trapped vortices formed from the plasma actuation are planned to create a mirror image velocity profile of the natural shedding one, as shown in Figure 19. Although the asymmetric unsteady actuation delays and reduces the separation region, it is not very effective in the lift reduction.

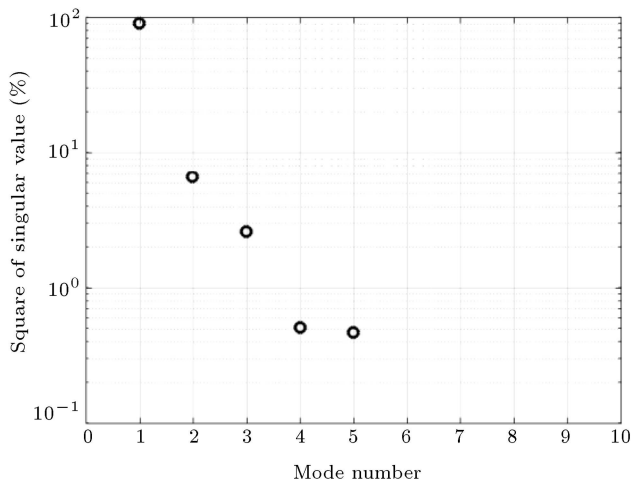


Figure 14. Eigenvalues of the harmonic in-phase plasma actuation with 50% duty cycle.

Figure 20 presents the snapshots of the velocity field for the unsteady harmonic out-phase plasma activated from the opposite side of natural shedding. It is clear that the plasma initiates a vortex from the upper side that continues to grow with the natural vortex formed from the lower side. However, this smaller vortex sheds faster at $t = 0.05421s$. The natural vortex starts to form from the upper side forcing the momentum source through plasma to switch to the lower side to create an induced vortex to oppose it and the cycle is repeated. Due to the smaller size of the induced vortex, the shear layer of the induced vortex

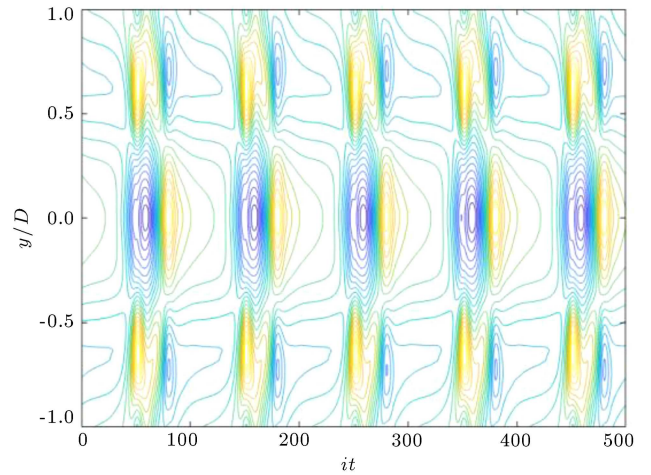


Figure 16. Reconstructed temporal evolution of velocity field by 2 POD modes for harmonic in-phase plasma actuation with 50% duty cycle.

does not cut the natural vortex along the symmetry axis and is separated sooner. Then, instead of a symmetric velocity pattern in a half shedding cycle, a semi-symmetric pattern is observed. Thus, the smaller vortex modifies the wake flow structure and weakens the Karman vortex shedding, while contrary to the in-phase pulsed actuation, out-phase excitation with the specified strength cannot form a symmetric wake pattern, indicating that by adjusting the optimum location of the plasma actuator and its strength in order to create a vortex similar in size and position

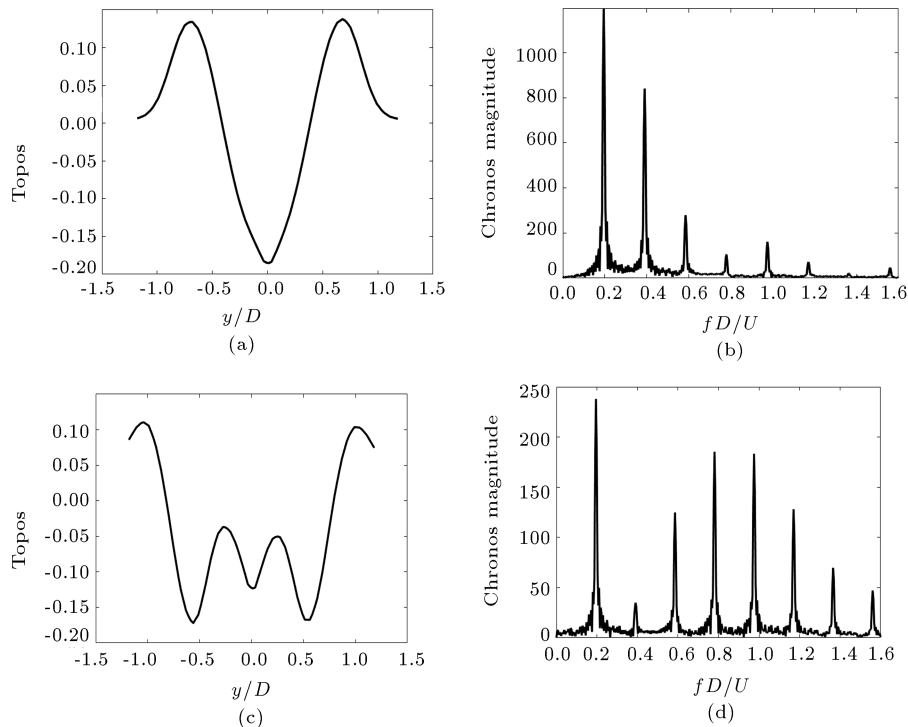


Figure 15. Topos and Chronos of the two dominant POD modes for harmonic in-phase plasma actuation with 50% duty cycle.

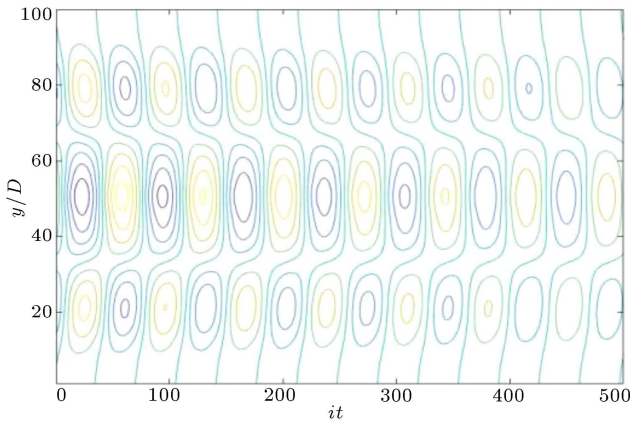


Figure 17. Reconstructed velocity field using 2 primary DMD modes for harmonic in-phase plasma actuation with 50% duty cycle.

to the natural formed vortex, it is possible to decrease the lift force with minimum energy consumption.

Figure 21 shows that in harmonic out-phase case, two modes contain 0.8 fraction of the total fluctuating kinetic energy. In the velocity spectral measurements, the dominant peak is observed at $St = 0.4$, which matches the lift force frequency. Although there is a competition between modes S and K in Figure 22, their interaction leads to the asymmetric wake flow structure. The global flow field reconstructed based on the two primary modes, given in Figure 23, exhibits an asymmetric pattern since the harmonic out-phase excitation could not energize the 2nd symmetric mode sufficiently. Then the harmonic out-phase actuation has a limited effect on the flow characteristics, compared to the in-phase excitation.

The DMD modes capture the relevant frequencies of the two stable modes for the harmonic out-phase plasma actuation. The first dominant non-dimensional frequency is at $St = 0.4$ with an asymmetric wake pattern, while the second one is at $St = 0.8$ with the associated symmetric spatial structure. Due to the lower energy of the mode S , the reconstructed wake pattern from these two modes is asymmetric, as shown

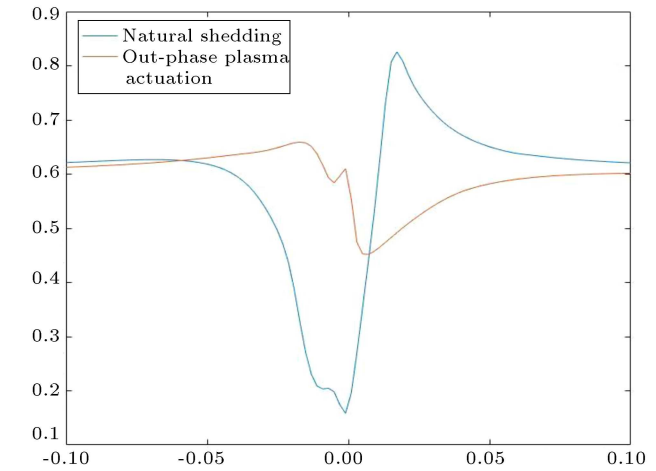
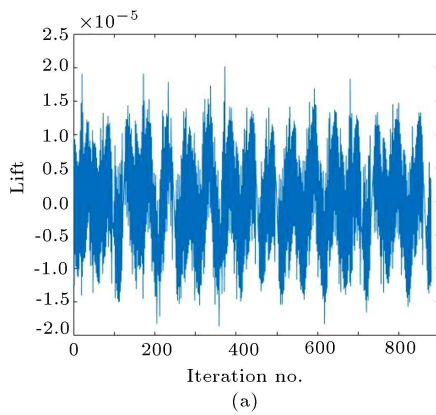


Figure 19. Velocity profile modification due to the harmonic out-phase plasma actuation.

in Figure 24. It matches well with the POD flow field observed in Figure 23, while the POD velocity field has a highly detailed vortical structure owing to the presence of various harmonics. The DMD flow field has a smaller vortical structure than the in-phase excitation velocity field, as given in Figure 11.

The superharmonic out-phase actuation with the excitation frequency of $f_e = 5f_s$ is selected for further study. The periodic behavior in the lift force is clear in Figure 25 where the main peak located at $St = 1$ represents the excitation frequency. The momentum source is asymmetrically exerted, switching between the upper and lower sides of the cylinder five times faster than the natural vortex shedding frequency. Figure 26 indicates that the higher excitation frequencies can delay the B.L. separation leading to the lower lift force in comparison to no control case. However, the vortex shedding is not suppressed although the width of this region is reduced. A comparison of the lift force in Figures 12, 18, and 25 revealed that the harmonic excitation reduced the vortex shedding more efficiently.

For the out-phase actuation with the frequency of $f_e = 5f_s$, two primary POD modes account for ap-

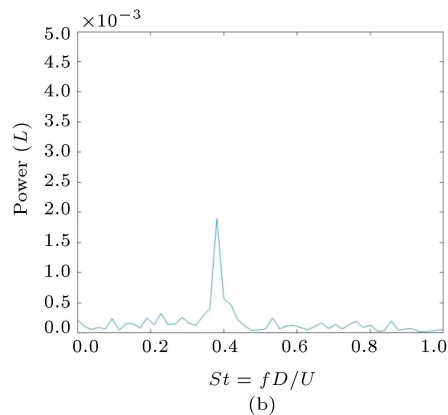


Figure 18. The lift force with its spectra for harmonic out-phase plasma actuation.

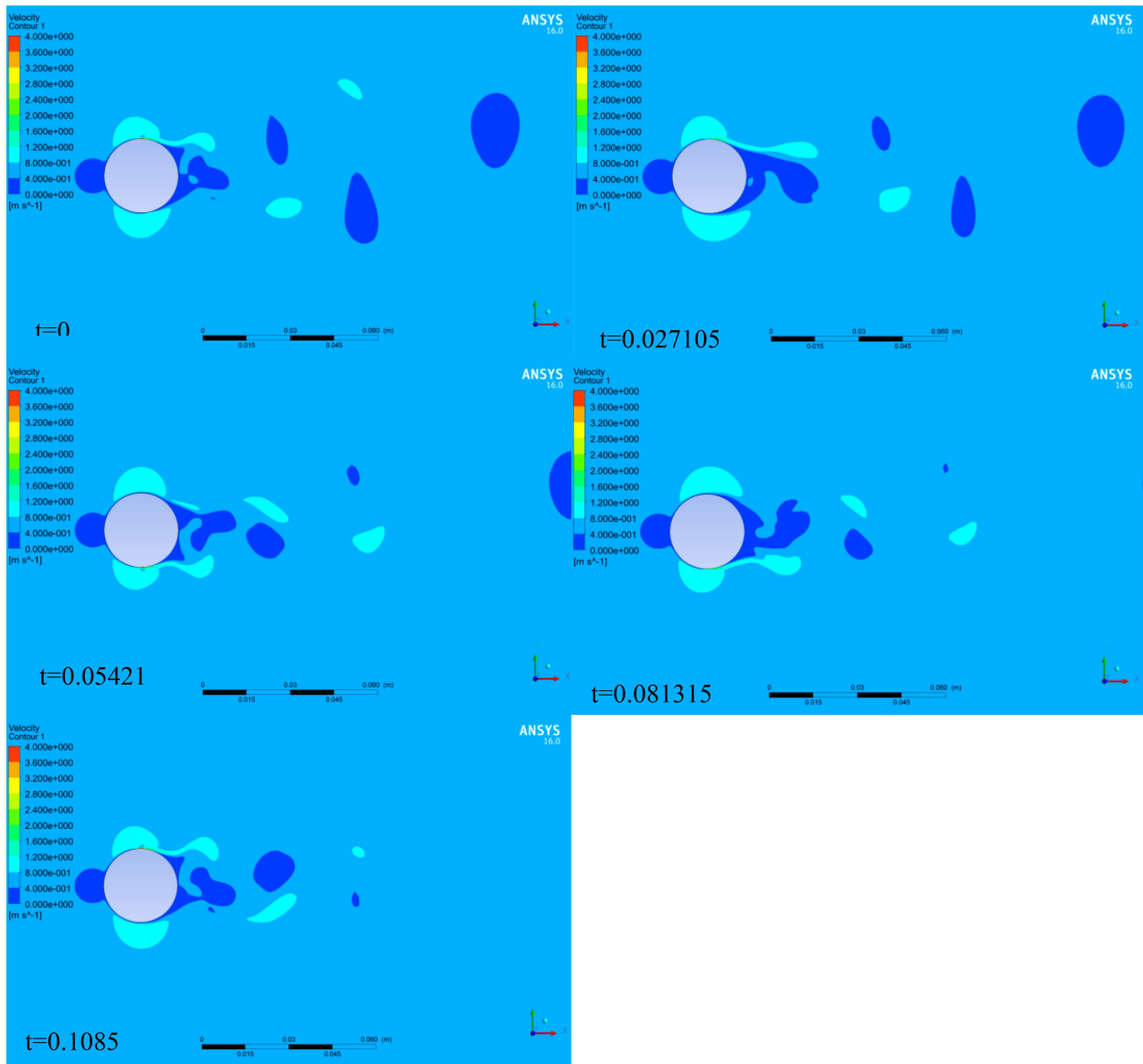


Figure 20. The snapshot of velocity field over a shedding cycle for pulse harmonic out-phase plasma actuation.

proximately 80% of the total fluctuating kinetic energy, as shown in Figure 27. The main modes exhibited little difference compared to the natural shedding case where the competition between modes K and S is clearly detected in Figure 28(a) and (c). The power spectra of the first mode show the main frequency at $St = 1$, corresponding to the excitation frequency, while the second mode has the main peak at $St = 2$ due to the alteration occurred by plasma actuation. The deduced wake structure given in Figure 29 shows that the asymmetric mode still overcomes the symmetric one, and superharmonic out-phase excitation cannot change the flow spatial symmetry. This actuation only makes the wake region thinner; however, it is not efficient enough to considerably decrease the lift.

The stability of superharmonic plasma actuation modes is characterized by DMD method. Figure 30

represents the asymmetric spatial pattern with smaller vortical structures than those of the harmonic cases. The first DMD mode complex eigenvalue is $0.9566 + 0.2475i$ pertinent to $St = 0.77$, while the second mode with complex eigenvalue equals $0.09159 + 0.329i$ which corresponds to $St = 1$, both with asymmetric pattern corresponding to the mode K with a monotonic amplitude decay rate.

The first mode frequency does not exist in the POD mode harmonics, while the second mode frequency matches the first POD peak. The nonlinear interaction between the modes K and S induced from the superharmonic out-phase actuation leads to the frequency of $St = 0.77$. However, since no mechanism gives energy to the symmetric mode S , its energy is reduced, hence higher DMD modes. Since the excitation frequency is high, the smaller wake structure is

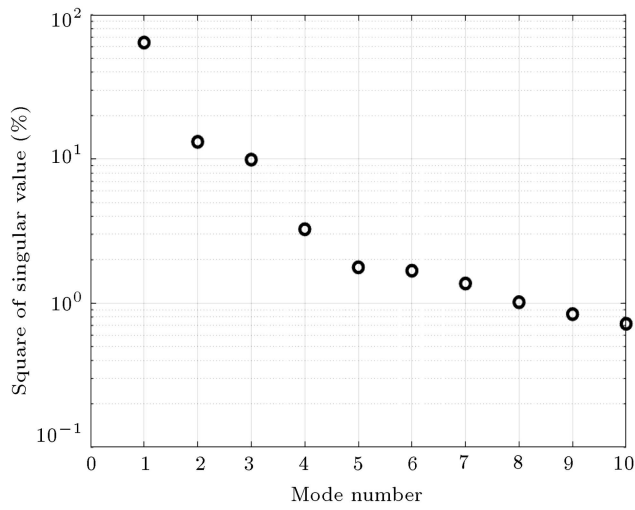


Figure 21. Eigenvalues of the unsteady harmonic out-phase plasma actuation.

formed which diminishes due to the amplitude decaying rate. Then, although the mode S is extracted from the POD analysis as the second mode consisting around 10% of fluctuating kinetic energy, high decaying rate calculated by the DMD method causes them to the higher modes with lower stability.

Due to the periodic nature of the vortex shedding, the lift and drag experience oscillation. At the specific time of $t = 10s$, the lift-to-drag ratio was calculated for all cases. According to Figure 31, the harmonic in-phase actuation can most effectively

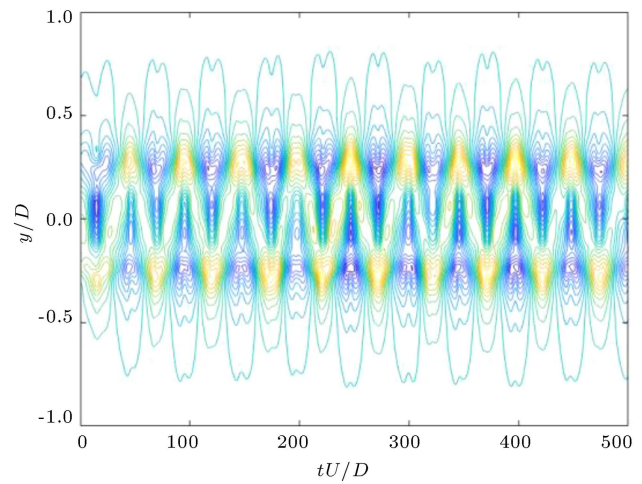


Figure 23. Reconstructed temporal evolution of velocity field using two primary POD modes for harmonic out-phase plasma actuation.

control the vortex shedding. Upon the harmonic in-phase plasma activation, the wake flow is modified due to the formation of two symmetric vortices reducing the lift coefficient considerably while the drag coefficient variation is negligible, compared to the no-control case.

In the harmonic out-phase excitation, the induced vortex is smaller than the natural one, forming a quasi-symmetric pattern that is not much effective in lift reduction, while the drag force is almost equal to that in the harmonic in-phase case. The superharmonic actuation reduces the wake region width, which decreases

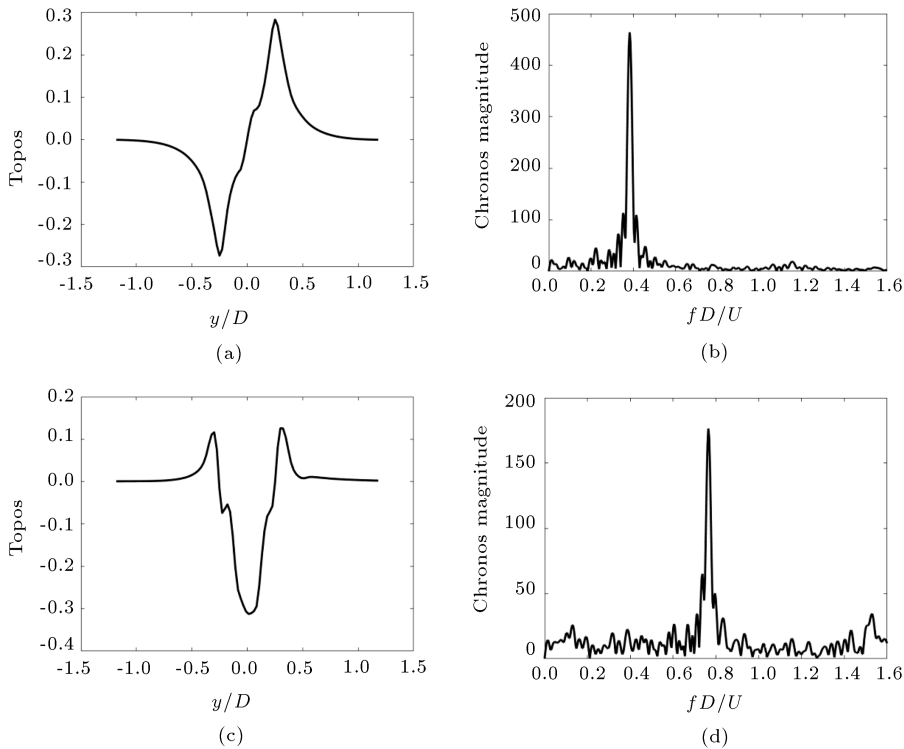


Figure 22. Topos and Chronos of two dominant POD modes for unsteady harmonic out-phase plasma actuation.

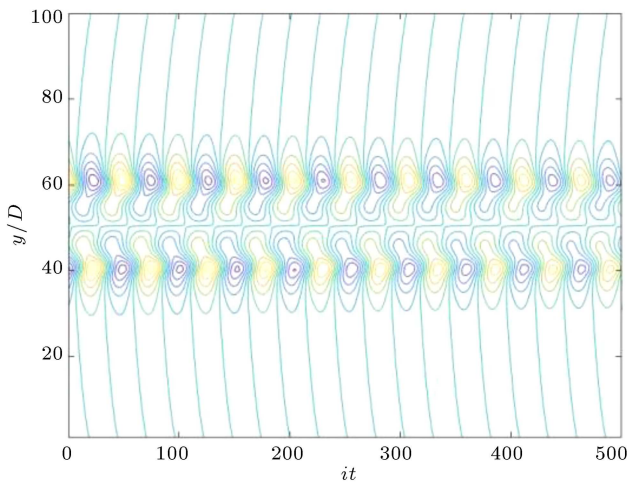


Figure 24. Reconstructed velocity field using two primary DMD modes for harmonic out-phase plasma actuation.

the lift and drag simultaneously; however, its energy consumption is much higher.

The actuation strength value, as an important parameter for the flow aerodynamics, is determined by setting the proper frequency and amplitude of the generated signal in experiments and it equals the body force value in the numerical model. Although the numerical body force and experimental plasma strength from a quantitative point of view are predicted in terms

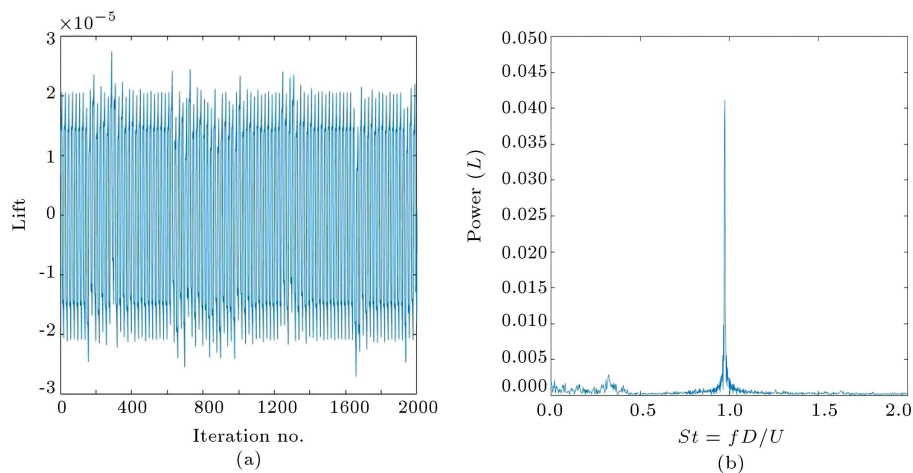


Figure 25. The lift force with its spectra for pulse out-phase plasma actuation with $f_e = 5f_s$.

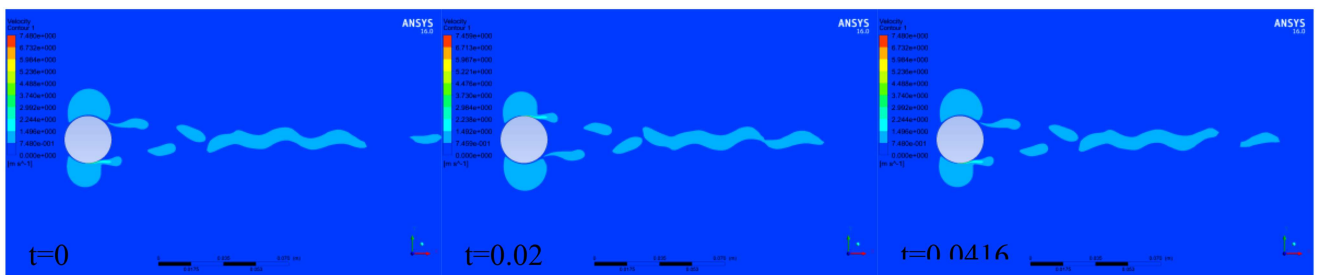


Figure 26. The snapshots of velocity field over an excitation cycle for pulse out-phase plasma actuation with $f_e = 5f_s$.

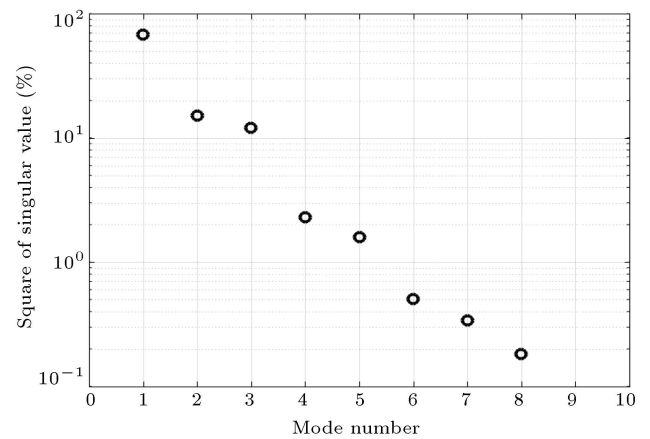


Figure 27. Eigenvalues of the unsteady out-phase plasma actuation with $f_e = 5f_s$.

of the velocity magnitude and qualitatively from the velocity profile trends, there remains an uncertainty in the equivalence of the experimental actuator strength and numerical body due to the assumptions made in the numerical simulation. DMD is applied to the data sequences of the PIV measurements of the wake flow from 180 images to extract the stable flow structures through post-processing in Dantec software to validate the numerical results. The sampling frequency due to the Nyquist criterion should be at least twice the natural shedding frequency to resolve the dominant

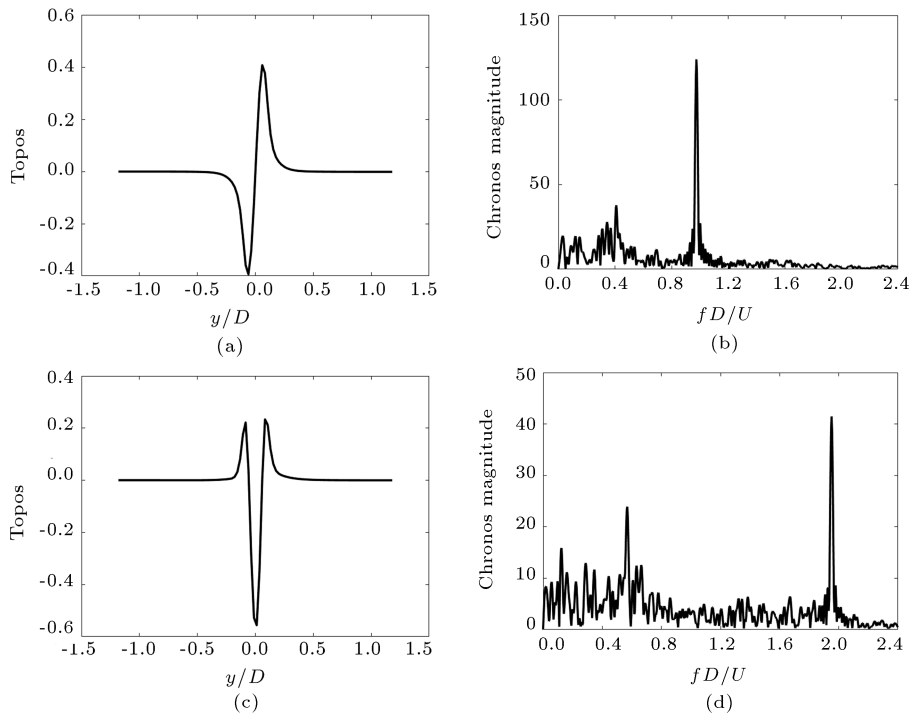


Figure 28. Topos and Chronos of two dominant POD modes for unsteady out-phase plasma actuation with $f_e = 5f_s$.

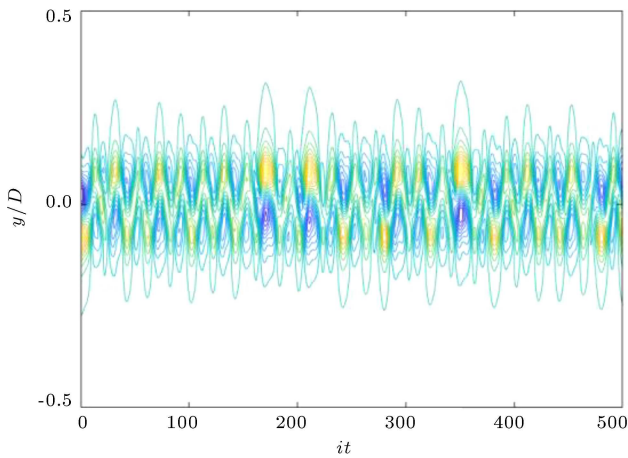


Figure 29. Reconstructed temporal evolution of velocity field using two primary POD modes for out-phase plasma actuation with $f_e = 5f_s$.

temporal dynamic mode. In these experiments, it is three times the Nyquist cut-off frequency in the unsteady harmonic cases. Nevertheless, the fast processes in superharmonic out-phase actuation are sampled at random amplitudes and cannot be captured with this sampling frequency. The time averaged velocity vector field for the uncontrolled flow based on 180 snapshots, including around 55 cycles, is presented in Figure 32. The Karman vortex shedding can be detected through 2D PIV measurements for unactuated flow. The effect of plasma actuation on the velocity field for the harmonic unsteady in-phase and out-phase plasma actuation cases was also experimentally assessed.

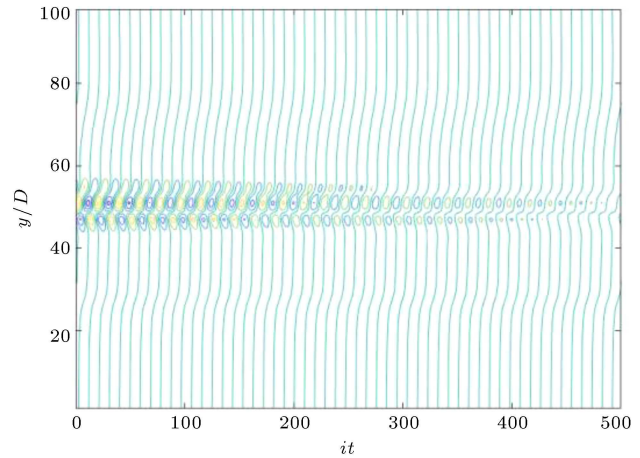


Figure 30. Reconstructed velocity field using two DMD modes for superharmonic out-phase plasma actuation.

The effect of the harmonic in-phase actuation was studied by observing the velocity vector field, velocity contours, and streamlines. The large scale symmetric vortical flow structure is the most dominant dynamic mode with a natural shedding oscillatory period over the streamwise direction in the investigation window of Figure 33. The jet induced by in-phase pulsed actuation deflects the shear layer by generating two vortices simultaneously shedding from the lower and upper sides of the cylinder with the opposite sign, as observed in the vorticity contour in Figure 34(a).

These vortices interacted with the shear layer in the recirculation region, thus inhibiting the roll up of the shear layer and, consequently, redirected the shear

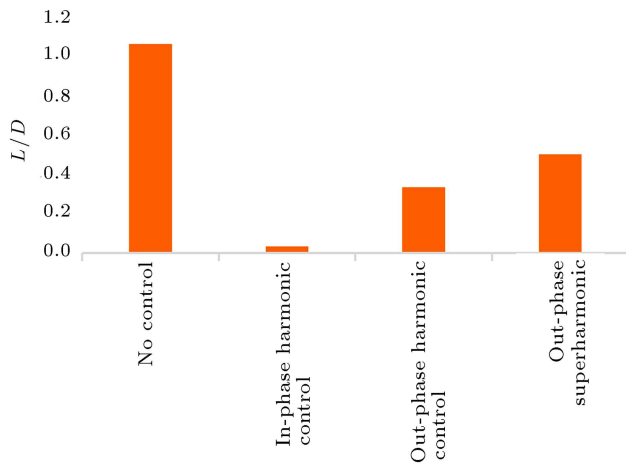


Figure 31. Lift to drag ratio of the cylinder for different cases at $t = 10s$.

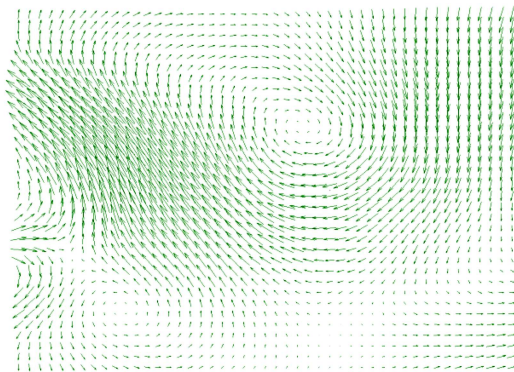


Figure 32. Time-averaged velocity field for unactuated case.

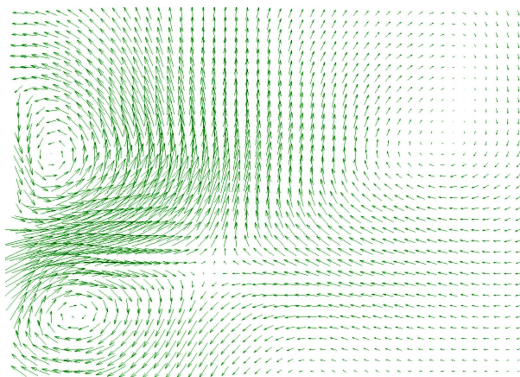


Figure 33. The velocity vector field for harmonic in-phase plasma actuation.

layer toward the centerline of the wake and closed the streamlines given in Figure 34(b) by forming a stagnation point where the interaction of two shear layers were blocked and vorticity cannot transfer to the recirculation area and make the streamlines almost symmetric.

The harmonic out-phase plasma actuation is observed from PIV velocity visualization in Figure 35.

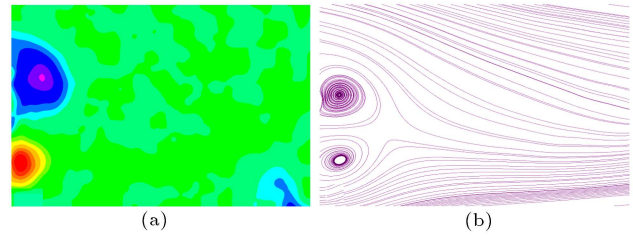


Figure 34. (a) Time-averaged velocity contour. (b) Streamlines for harmonic in-phase plasma actuation with 50% duty cycle.

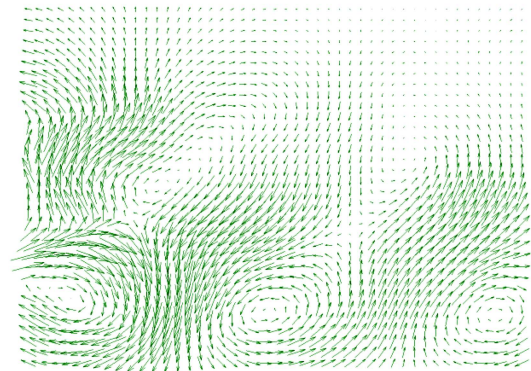


Figure 35. Time-averaged velocity field for harmonic out-phase plasma actuation.

The predominant wake structure is similar to the natural Karman shedding with little modification to the vortex structure due to the out-phase pulsed actuation. The asymmetric velocity field validates the numerical result.

6. Conclusion

In the present work, the influence of frequency and phase difference of plasma actuation on the wake flow symmetry for $Re = 1000$ were numerically investigated and validated through the conducted experiments. The forcing actuation was modeled as a slip-wall condition in the CFD for the unsteady in-phase excitation with 50% duty cycle and out-phase excitation at its resonant frequency as well as the fifth harmonic of the natural shedding frequency. The harmonic in-phase momentum addition led to symmetric velocity field, which dominated the asymmetric Karman shedding and reduced the lift coefficient considerably in comparison to no flow-control case. The harmonic out-phase actuation induced a smaller vortex simultaneously, while a natural vortex formed on the other side in order to create a symmetric pattern. Due to the lower strength and improper position of plasma, the symmetric pattern was not formed. The induced quasi-symmetric velocity profile was not an exact mirror image of the natural one, which weakened the shear layer, but was not strong enough to decrease the lift coefficient significantly. The application of the plasma

actuation with proper phase difference and optimum position at specific strength power could generate an induced velocity profile with a higher amplitude, which can decrease the lift efficiently with minimum energy consumption. In the superharmonic out-of-phase actuation, the reduction of the separation region resulted from momentum injection into the boundary layer faster than natural shedding, which delayed the separation. The formed vortices had smaller sizes and, therefore, a narrower wake region. However, the lift magnitude reduction was not considerable. The main difference between harmonic and superharmonic excitations was that at a natural shedding frequency, the turbulent structure of the flow was resonated to create a symmetric velocity pattern, leading to a lift reduction, while at superharmonic actuation, only the momentum injection energized the boundary layer structure delaying the boundary layer separation.

The POD functions were based on spatial orthogonality that extracted the most energetic modes, while the DMD was based on the temporal orthogonality identifying the stable modes. DMD decouples each mode specific frequency leading to the modes interaction dynamics predictable. Due to the similar behavior of the dominant modes to CFD results, the reduced order velocity field was employed to study the flow dynamics and design an active control. It was observed that plasma location, excitation frequency, duty cycle, and phase difference between plasma actuators affected the velocity patterns.

Acknowledgment

This research did not receive any specific grant from funding agencies in the public, commercial, or not-for-profit sectors. The experiments were done in FIV Lab at Polytechnique Montreal.

Nomenclature

a_i	Chronos
A	Velocity field matrix
a	Acceleration, m/s
C	Covariance matrix
f	Frequency, Hz
f_v	Body force per unit volume, N/m ³
$f(y)$	Symmetric eigenfunctin
$g(y)$	Asymmetric eigenfunctin
$K(t)$	Asymmetric mode amplitude
KE	Kinetic energy
$SO(2)$	Translational symmetry
Re	Reynolds number
$S(t)$	Symmetric mode amplitude

St	Strouhal number
S^1	Phase shift symmetry
$u_{0,1}$	Initial and induced velocities respectively, m/s
v	Velocity, m/s
v'	Velocity perturbation, m/s
v_i	Eigenvector
W	Eigenvector of square matrix
X	Velocity field matrix
$Z_2(\kappa)$	Reflection symmetry

Greek symbols

$\alpha_i + i\delta_i$	Complex bifurcation parameters of symmetric mode S
$\beta_i + i\mu_i$	Complex bifurcation parameters of asymmetric mode K
$\eta_i + i\kappa_i$	Complex bifurcation parameters of asymmetric mode K
$\xi_i + i\gamma_i$	Complex bifurcation parameters of asymmetric mode K
θ	Right singular vector
λ	Wavelength, m
μ_i	Eigenvalue
ρ	Density, kg/m ³
Σ	Eigenvalue matrix
σ_i	Mode growth/decay rate
τ	Time period, s
φ_i	Topos
ω	Angular velocity, rad/s

References

1. Artana, G., Sosa, R., Moreau, E., and Touchard, G. "Control of the near-wake flow around a circular cylinder with electrohydrodynamic actuators", *Exp. Fluids*, **35**(6), pp. 580–588 (2003). DOI: 10.1007/s00348-003-0704-z.
2. Hyun, K.T. and Chun, C.H. "The wake flow control behind a circular cylinder using ion wind", *Exp. Fluids*, **35**(6), pp. 541–552 (2003). DOI: 10.1007/s00348-003-0668-z.
3. Post, M.L. and Corke, T.C. "Separation control on high angle of attack airfoil using plasma actuators", *AIAA J.*, **42**(11), pp. 1–11 (2004). DOI: 10.2514/1.2929.
4. Xu, X., *Plasma Actuation for Boundary Layer Separation Control in Engine Ducts*, Polytechnique de Montreal (2011).
5. West IV, T.K. and Hosder, S. "Numerical investigation of plasma actuator configurations for flow separation control at multiple angles of attack", *Int. J. Flow Control*, **5**(1), pp. 25–46 (2013). DOI: 10.1260/1756-8250.5.1.25.
6. Chen, J.L. and Liao, Y.H. "Effects of an annular plasma actuator on a co-flow jet downstream of a bluff-body", *Appl. Therm. Eng.*, **192**, pp. 1–10 (2021). DOI: 10.1016/j.applthermaleng.2021.116975.

7. Sato, M., Asada, K., Nonomura, T., et al. “Mechanisms for turbulent separation control using plasma actuator at Reynolds number of 1.6×10^6 ”, *Phys. Fluids*, **31**(9) (2019). DOI: 10.1063/1.5110451.
8. Huang, G., Dai, Y., Yang, C., et al. “Effect of dielectric barrier discharge plasma actuator on the dynamic moment behavior of pitching airfoil at low Reynolds number”, *Phys. Fluids*, **33**(4) (2021). DOI: 10.1063/5.0048235.
9. Vaddi, R.S., Sota, C., Mamishev, A., et al., *Active Flow Control of NACA 0012 airfoil using Sawtooth Direct Current Augmented Dielectric Barrier Discharge Plasma Actuator*, Prepr. ArXiv (2020).
10. Guoqiang, L., Weiguo, Z., Yubiao, J., et al. “Experimental investigation of dynamic stall flow control for wind turbine airfoils using a plasma actuator”, *Energy*, **185** (2019). DOI: 10.1016/j.energy.2019.07.017.
11. Guoqiang, L. and Shihe, Y. “Large eddy simulation of dynamic stall flow control for wind turbine airfoil using plasma actuator”, *Energy*, **212** (2020). DOI: 10.1016/j.energy.2020.118753.
12. Moreau, E., Debien, A., Breux, J.M., and Bernard, N. “Control of a turbulent flow separated at mid-chord along an airfoil with DBD plasma actuators”, *J. Electrostat.*, **83**, pp. 1–8 (2016). DOI: 10.1016/j.elstat.2016.08.005.
13. Dedrick, J., Im, S., Cappelli, M.A., et al. “Surface discharge plasma actuator driven by a pulsed 13.56 MHz-5 kHz voltage waveform”, *J. Phys. D. Appl. Phys.*, **46**(40), pp. 1–13 (2013). DOI: 10.1088/0022-3727/46/40/405201.
14. Choi, H., Jeon, W.P., and Kim, J. “Control of flow over a bluff body”, *Annual Review of Fluid Mechanics*, **40**, pp. 113–139 (2008). DOI: 10.1146/annurev.fluid.39.050905.110149.
15. Nati, G., Kotsonis, M., Ghaemi, S., et al. “Control of vortex shedding from a blunt trailing edge using plasma actuators”, *Exp. Therm. Fluid Sci.*, **46**, pp. 199–210 (2013). DOI: 10.1016/j.exptthermfluidsci.2012.12.012.
16. Brauner, T., Laizet, S., Benard, N., et al. “Modelling of dielectric barrier discharge plasma actuators for direct numerical simulations”, pp. 1–17 (2016). DOI: 10.2514/6.2016-3774.
17. D’Adamo, J., Sosa, R., and Artana, G. “Active control of a backward facing step flow with plasma actuators”, *J. Fluids Eng. Trans. ASME*, **136**(12), pp. 1–37 (2014). DOI: 10.1115/1.4027598.
18. Sosa, R., D’Adamo, J., and Artana, G. “Circular cylinder drag reduction by three-electrode plasma actuators”, in *Journal of Physics: Conference Series*, **166**, pp. 1–14 (2009). DOI: 10.1088/1742-6596/166/1/012015.
19. Rodrigues, F., Mushyam, A., Pascoa, J., et al. “A new plasma actuator configuration for improved efficiency: The stair-shaped dielectric barrier discharge actuator”, *J. Phys. D. Appl. Phys.*, **52**(38), pp. 1–22 (2019). DOI: 10.1088/1361-6463/ab2584.
20. Mohammad-Reza Pendar, J.C.P. “Numerical investigation of plasma actuator effects on flow control over a three-dimensional airfoil with a sinusoidal leading edge”, *J. Fluids Eng. Trans. ASME Fluids Eng.*, **144**(8), pp. 1–17 (2022). DOI: [https://doi-org.ezp3.semantak.com/10.1115/1.4053847](https://doi.org/ezp3.semantak.com/10.1115/1.4053847).
21. Zhang, X. and Zong, H. “Vortex shedding frequency scaling of coherent structures induced by a plasma actuator”, *AIAA J.*, **60**(2), pp. 1067–1076 (2022). DOI: 10.2514/1.J060903.
22. Emori, K., Kaneko, Y., Nishida, N. “Influence of main flow on vortex structure generated by burst mode actuation of DBD plasma actuator”, *AIAA J.*, **70**, pp. 115–129 (2022). DOI: <https://doi.org/10.2514/6.2022-2595>.
23. Nabatian, N. and Mureithi, N.W. “Bifurcation and stability analysis with the role of normal form symmetries on the harmonic streamwise forced oscillation of the cylinder wake”, *Eur. J. Mech. B/Fluids*, **70** (2018). DOI: 10.1016/j.euromechflu.2018.02.003.
24. Nabatian, N. and Mureithi, N.W. “Lock-on vortex shedding patterns and bifurcation analysis of the forced streamwise oscillation of the cylinder wake”, *Int. J. Bifurc. Chaos*, **25**(9) (2015). DOI: 10.1142/S0218127415300220.
25. Nabatian N. and Mureithi, N.W., *Bifurcation Analysis and the Role of Normal form Symmetries on the Harmonic Forced Inline Oscillation of the Cylinder Wake*, in American Society of Mechanical Engineers, Pressure Vessels and Piping Division (Publication) PVP, **4** (2016). DOI: 10.1115/PVP2016-63334.
26. Ergin, F.G., Watz, B.B., Erglis, K., et al. “Modal analysis of magnetic microconvection”, *Magneto-hydrodynamics*, **50**(4), pp. 339–352 (2014). DOI: 10.22364/mhd.50.4.1.
27. Xavier, P., Vandael, A., Godard, G., et al. “Simultaneous high-speed OH-PLIF and PIV measurements to study the flame dynamics in an acoustically self excited trapped vortex combustor”, *17th Int. Symp. Appl. Laser Tech. to Fluid Mech.*, **7**, pp. 7–10 (2014).
28. Klein, T.R., *Macroscopic Computational Model of Dielectric Barrier Discharge Plasma Actuators*, Air Force Institute of Technology (2006).

Biography

Negar Nabatian received her BSc and MSc degrees from Sharif University and her PhD from Polytechnique de Montreal University. Her research interests are FSI, reduced order models, combustion and heat transfer. She has worked as the Professor in the Faculty of Mechanical and Energy Engineering at Shahid Beheshti University since 2015.